RSC Advances

Check for updates

Comparative study of the impact of heat treatment on the microstructure, morphology, optical and dielectric properties of nanostructured Co–Mn ferrite

J. Othmani,[a] Ah. Dhahri, [iD] *[b] S. Hcini, [iD] [c] M. L. Bouazizi,[d] K. Khirouni,[e] E. Dhahri [iD] [a] and Benilde F. O. Costa[b]

Nanoscale materials are attracting a great deal of attention due to their exceptional properties, making them indispensable for many advanced applications. Among these materials, spinel ferrites stand out for their potential applications in electronic, optoelectronic, energy storage and other devices. This is why the development of a synthesis process combined with rigorous optimization of annealing conditions is provided to be an essential approach to control nanoparticle formation and fine-tuning their structural, morphological and functional characteristics. A new approach is proposed to tailor the multifunctional properties of cobalt–manganese ferrites by synthesizing a non-stoichiometric composition. The compound $Co_{0.33}Mn_{0.33}Fe_{2.33}O_4$, containing an excess of Fe in the B sites, was obtained by the coprecipitation method combined with controlled annealing treatments. This strategy allows for the synergistic adjustment of structural, morphological, optical, and dielectric properties, and establishes a direct link between microstructural evolution and improved device performance. X-ray diffraction analysis confirmed the formation of a single-phase cubic spinel phase. The average crystallite size increased from 28 nm to 31 nm with higher annealing temperatures, indicating improved crystallinity. Morphological analysis by scanning electron microscopy revealed a significant grain growth and a reduction in irregular grain boundaries, which can minimize charge carrier scattering (beneficial for high-frequency capacitor and microwave device applications). UV-visible-near infrared spectroscopy showed a decrease in the optical band gap from 3.13 eV to 2.45 eV with increasing temperature, indicating a change in electronic structure. This variation suggests that the material can be integrated into devices such as transistors, modulators or optical switches. Finally, dielectric measurements revealed a high dielectric constant with low losses, underlining the potential of this material for applications in high-performance components.

1. Introduction

Spinel ferrites with the general formula AB_2O_4 are the subject of extremely intensive research due to the wide range of potential technological applications, this includes energy storage devices (supercapacitors and batteries), optical systems, liquid cooling systems, and gas sensors. It also includes various biomedical applications, such as contrast agents for magnetic resonance imaging (MRI), magnetic-guided drug delivery, and cancer[1–16]

[a]*Laboratoire de Physique Appliquée, Faculté des Sciences, Université de Sfax, Tunisia*

[b]*University of Coimbra, CFisUC, Physics Department, Rua Larga, P-3004-516 Coimbra, Portugal. E-mail: ahmed.dhahri@live.fr*

[c]*Laboratory of Advanced Multifunctional Materials and Technological Applications, Faculty of Science and Technology of Sidi Bouzid, University of Kairouan, Tunisia*

[d]*Department of Mechanical and Energy Engineering, College of Engineering, Imam Abdulrahman Bin Faisal University, Dammam, 1982, Saudi Arabia*

[e]*Laboratoire de Physique des Matériaux et des Nanomatériaux appliquée à l'Environnement, Faculté des Sciences de Gabès, Université de Gabès, Tunisia*
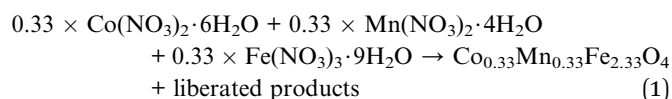
Cobalt ferrite ($CoFe_2O_4$) is one of the best-known spinel ferrites. Its interesting dielectric, optical, structural and morphological properties make it a valuable material for a variety of applications. Kershi *et al.*[17] observed in their extensive study of cobalt ferrite that it exhibits low values for some parameters such as lattice constant a, mean crystallite size D, absorption coefficient α, refractive index n, dielectric constant ε' and conductivity. On the other hand, high values were found for the direct and indirect energy gaps, elastic moduli (E, B, G) as well as the Debye temperature (θ_D). These results suggest that the material can be used in a variety of potential applications, including high-temperature and high-pressure environments. With an energy gap below 2 eV, the material is particularly suitable for photo-Fenton applications in the visible light range and for some magnetic storage systems for specific applications. In their studies based on theoretical calculations by DFT concerning optical properties, Elham Gharibshahi *et al.*[18] identified various approaches that will allow design engineers to adapt

$CoFe_2O_4$ nanoparticles for different possible applications, including in electronic devices, sensors, and microwave devices. Chen et al.[13] studied the properties of cobalt ferrite. They found that this type of material exhibited magnetostriction in excess of 200 ppm while having a high d_{33} coefficient of $1.3 \times 10^{-9}\,A^{-1}m$ at low applied field strength. These results make the compound a promising candidate for torque sensors, various other magnetostrictive sensor and actuator applications. Previous studies by Kai Wei et al.[8] revealed that $CoFe_2O_4$ exhibits N-type gas sensing behavior, characterized by a decrease in resistance when exposed to a reducing gas. Sensors based on $CoFe_2O_4$ have proven effective for ethanol detection, operating at a temperature of 200 °C. By doping cobalt ferrites with metallic elements, researchers can also obtain new properties. This is particularly the case with manganese. Studies conducted in recent years by Zhang et al.[14] have shown that doping cobalt ferrite with Mn, at a concentration of between 10 and 20%, significantly increases magnetic anisotropy while improving relative dielectric permittivity from 15 to 25 at a frequency of 1 MHz. These modifications optimize the magnetic and dielectric performance required for miniaturized spintronic devices. Furthermore, Singh et al.[19] highlighted the effect of manganese on the photoluminescent properties of cobalt ferrite nanoparticles, characterized by an emission peak centered at 520 nm, the intensity of which is modulated according to the Mn content. This photoluminescent modulation capability makes these materials particularly suitable for optoelectronic applications, particularly in the field of sensors. These alterations in properties are attributable to a redistribution of cations within the spinel structure, thereby modifying magnetic exchange interactions and the local electronic structure. Kumar et al.[20] pointed out that the use of advanced synthesis techniques, such as the solvothermal method, allows precise control of the size of the nanoparticles, generally maintained between 15 and 25 nm, which facilitates the adjustment of functional properties according to the specific needs of the intended applications. Atif et al.[21] examined the effect of Mn substitution on the properties of a series of $Co_{(1-x)}Mn_xFe_2O_4$ ferrites ($0.0 \leq x \leq 0.4$) synthesized by the solid-state reaction method. They observed an increase in the lattice parameter, as well as a decrease in density deduced from X-ray diffraction and average grain size with increasing Mn(x) content. The electrical study reveals a considerable increase in total resistance and grain and grain boundary resistance with increasing Mn content. This is linked to changes in cation distribution and microstructure. Dielectric properties also undergo strong variations under the effect of cation redistributions and morphological evolutions associated with the increase in Mn concentration. These observations suggest that it is possible to control the structural and electrical properties by modifying the Mn ion content in cobalt ferrite. However, the high resistance values of these samples could make them suitable for potential future use in high-frequency applications. P. Sowjanya et al.[22] demonstrated that the $Ni_{0.5}Co_{0.5}Fe_2O_4$ compound exhibits higher sensitivity to aging at low magnetic fields, which constitutes a limitation for certain applications. However, this characteristic can be exploited advantageously in devices such as magnetic actuators and transducers, where dynamic response is paramount. Graphene-based Sm-doped cobalt ferrite nanoparticles were developed by Rania Ramadan et al.[23] Analyses show that this sample exhibits antibacterial activities against both Gram-positive and Gram-negative bacteria, with inhibition zones reaching 12–14.5 mm in diameter. In addition, the sample demonstrated a high adsorption capacity for Pb^{2+}, with a maximum removal efficiency of 99.8%. These results suggest that nanoscale samples of graphene-based Sm-doped Co-ferrite have potential for use as a bio-adsorbent and antibacterial agent. Practical and effective solutions for water disinfection are thus conceivable. Studies on the dielectric properties of aluminum-doped cobalt ferrite by Raghavender et al.[24] show lower values for dielectric constant and losses. It is therefore a promising material as a microwave absorber for high-frequency applications. Iron (Fe), a major component of ferrites, plays a key role in the crystal structure by occupying the tetrahedral and octahedral sites of the spinel lattice. This distribution influences the stability of the material as well as its electrical and optical properties, such as permittivity, dielectric loss, and response to wavelengths in the visible and near-infrared spectrum.[25] Heat treatments, such as annealing at different temperatures, are essential for controlling the microstructure, grain size, and ion distribution, which allows for fine tuning of the functional performance of ferrites.[1,2] Specifically, our study focuses on spinel ferrite of composition $Co_{0.33}Mn_{0.33}Fe_{2.33}O_4$, where Co^{2+} and Mn^{2+} ions were introduced in equal amounts, while a controlled excess of Fe^{3+} ions served to both stabilize the structure and maintain electrical neutrality. This specific cationic composition enables the material's functional properties to be modulated with great precision. More specifically, the study examines the impact of annealing temperature on various properties, such as structure, morphology, optical and dielectric properties, with a view to optimizing the performance of this material in optoelectronic applications and in dielectric components.

2. Materials and methods

$Co_{0.33}Mn_{0.33}Fe_{2.33}O_4$ compound is synthesized by the chemical coprecipitation method using as precursors $Fe(NO_3)_3\cdot9H_2O$, $Mn(NO_3)\cdot4H_2O$ and $Co(NO_3)_2\cdot6H_2O$, which react following the chemical reaction (1).

$$0.33 \times Co(NO_3)_2\cdot6H_2O + 0.33 \times Mn(NO_3)_2\cdot4H_2O$$
$$+ 0.33 \times Fe(NO_3)_3\cdot9H_2O \rightarrow Co_{0.33}Mn_{0.33}Fe_{2.33}O_4$$
$$+ \text{liberated products} \qquad (1)$$

Aqueous solutions are prepared by dissolving each chemical compound in distilled water (0.2 molar ($Fe(NO_3)_2\cdot9H_2O$) in 100 ml distilled water, 0.015 molar ($Mn(NO_3)_2\cdot4H_2O$) in 100 ml distilled water and 0.085 molar ($Co(NO_3)_2\cdot6H_2O$) in 100 ml distilled water). Then the solutions are mixed and stirred at 400 rpm at 80 °C for two hours to obtain a homogeneous product. The aqueous solution of the co-precipitant (NaOH) is simultaneously prepared in distilled water (0.5 molar NaOH in 100 ml distilled water) and sprayed drop by drop into the homogeneous solution under stirring (400 rpm) at 80 °C, until

a final pH of 10.0 ± 0.1 is reached (continuous measurement with a calibrated pH meter). The heating process is stopped after about 50 min and stirring is carried out for another two hours. The obtained precipitate was washed five to six times using distilled water and then oven-dried at 80 °C for 24 hours. The mixture was calcined at two temperatures (300 °C and 600 °C) for six hours, then ground for two hours. The resulting powder was then pressed into a pellet. The final compound was analyzed structurally, morphologically, dielectrically and optically. The crystalline structure was analyzed by X-ray diffraction (XRD) at room temperature in the angular range from 10° to 90°. This analysis was used to study the crystalline nature and phase purity of the ferrites. Morphology was examined using field emission scanning electron microscopy. Optical data was collected using a UV-visible-NIR spectrophotometer to determine the gap energy. Dielectric measurements were made using an impedance bridge over a frequency range of 80 Hz to 10 MHz, with a temperature range of 300 K to 640 K.

3. Results and discussions

3.1. X-ray diffraction analysis

X-ray diffractograms of our $Co_{0.33}Mn_{0.33}Fe_{2.33}O_4$ samples annealed at 300 °C and 600 °C were recorded at room
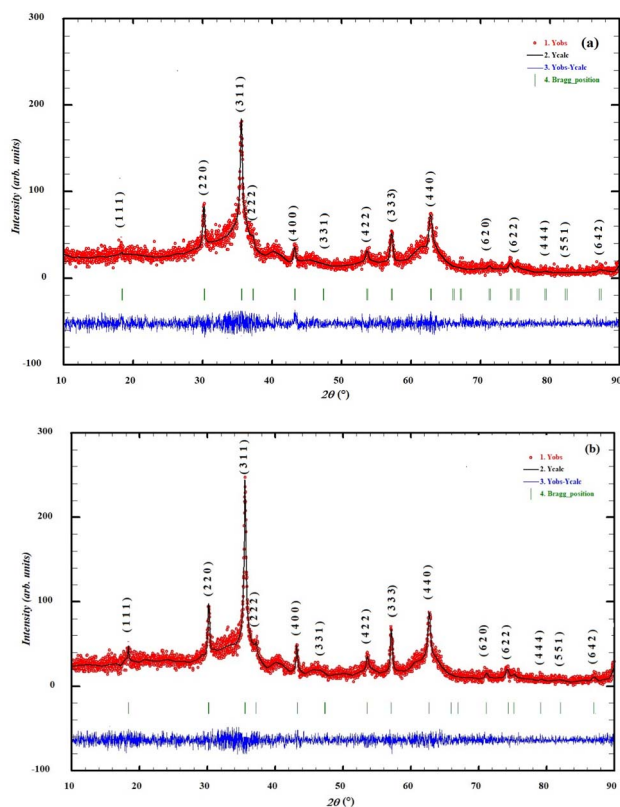
Table 1 Rietveld refinement parameters of Co300 and Co600, X-ray parameters, X-ray density (ρ_{X-ray}), bulk density (ρ_{exp})

Sample		Co300	Co600
Space group	$Fd\bar{3}m$		
Cell parameters	a (Å)	8.3581	8.3849
	V (A^3)	583.87	589.51
Agreement factors	χ^2 (%)	1.06	1.14
Average crystallite size (nm)	D_{sc}	28	32
Stress	ε	85×10^{-5}	34×10^{-5}
Density (g cm^{-3})	ρ_{X-ray}	6.62	6.55
Bulk density (g cm^{-3})	ρ_{exp}	6.48	6.36

temperature over an angular range of 10 to 90° as shown in Fig. 1. It is observed that all peaks are well indexed in the cubic system with the $Fd\bar{3}m$ space group. The absence of impurity peaks confirms the purity and the single phase of the studied samples. The intensity of the peaks increased with annealing temperature, indicating an improvement in crystallinity. All the structural data deduced from our Rietveld analysis are reported in our previous work.[26] In order to provide a comprehensive summary of the physical parameters extracted from the XRD data, including the space group, cell parameters, agreement factors, and the apparent and theoretical densities, these values are compiled and presented in Table 1. Analysis of the diffractograms using the Williamson–Hall method[27] allowed us to estimate the average size of the crystallites D as shown in Fig. 2, based on the equation (2):

$$\beta_{hkl} \cos \theta = k\lambda/D + 4\varepsilon \sin\theta \qquad (2)$$

where β_{hkl} denotes the width at half height, k represents a constant, θ indicates the diffraction angle, ε signifies the stress, while λ represents the wavelength of the X-ray (Kα line, λ = 1.541 836 Å). Estimates of average crystallite sizes and deformations are summarized in Table 1. As shown in this table, there is an increase in the average crystallite size from 28 nm to 32 nm, accompanied by a decrease in ε deformation from 85×10^{-5} to 34×10^{-5}, as the annealing temperature increases. These results confirm a significant improvement in crystallinity with increasing annealing temperature.[28]

3.2. Morphology proprieties

Morphological structure and grain size and shape have a major impact on the dielectric and optical properties of ferrites. In order to assess the surface finish and grain size, as well as any microstructural transformations, we carried out a microstructural analysis on the compound $Co_{0.33}Mn_{0.33}Fe_{2.33}O_4$ annealed at 300 °C (Co300) and 600 °C (Co600) for 6 hours.

3.2.1. Scanning electron microscopy (SEM) studies. Morphological studies of the samples annealed at 300 °C and 600 °C were carried out using field emission scanning electron microscopy (FESEM) with an accelerating voltage of 5 kV. Obtained images are shown in Fig. 3. It can be seen that the nanoscopic particles aggregate due to magnetic interactions between the atoms forming this material, giving the impression that the grain size is larger than expected. It should also be
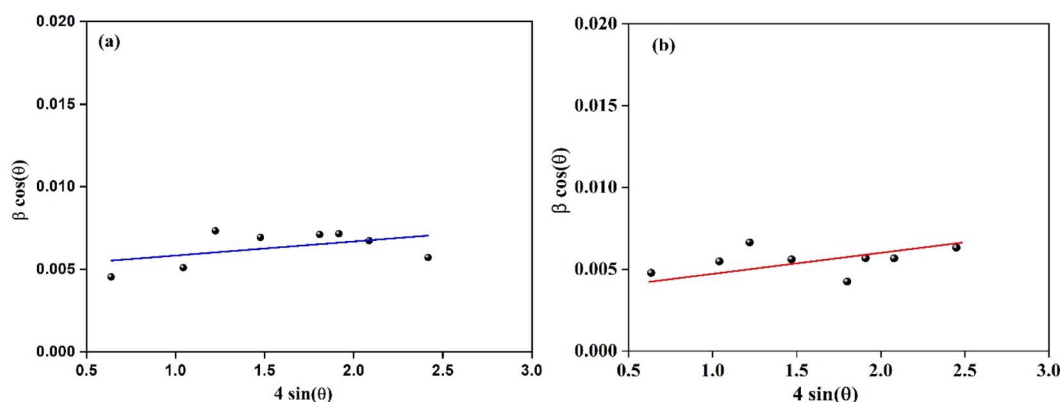

Fig. 1 Refined XRD patterns of $Co_{0.33}Mn_{0.33}Fe_{2.33}O_4$ annealed at 300 °C (a) and 600 °C (b) at room temperature. The red dotted line stands for the experimental data. The calculated data are represented by a black continuous line. The curve in blue shows the difference between the experimental and calculated patterns. The vertical bars in green indicate the Bragg positions.

Fig. 2 Williamson–Hall plots for samples Co300 (a) and Co600(b).

noted that the aggregation in the Co600 sample is more marked than in the Co300 sample, which can be attributed mainly to the increase in annealing temperature, which induces an increase in mobility.[29]

Average grain size was calculated using the ImageJ software. Grain diameters (D_1) were measured in the SEM image and the data was collected and evaluated using function (3):

$$f(D_1) = \left(\frac{1}{\sqrt{2\pi\sigma D_1}}\right)\exp\left[-\frac{\ln^2\left(\frac{D_1}{D_0}\right)}{2\sigma^2}\right] \quad (3)$$

where σ and D_0 represent the mean diameter obtained from SEM and scatter data for $Co_{0.33}Mn_{0.33}Fe_{2.33}O_4$ ferrite, respectively. As shown in the histogram in Fig. 4 statistical analysis of the grain diameters allows us to deduce the average grain size,

which is around 1.95 μm for Co300 and 3.53 μm for Co600. The agglomeration ratio also increases with the annealing temperature, rising from 3 for Co300 to 6 for Co600, indicating that the particles agglomerate easily at higher temperatures. This study shows that the grain size observed in the SEM micrographs for the two samples is larger than the size estimated from the XRD data. This indicates that each grain is made up of numerous crystallites[29] and that higher temperatures promote both grain growth and particle agglomeration.

3.2.2. Energy dispersive X-ray (EDX) analysis. EDX spectroscopy analysis (shown in Fig. 5) was used to assess the elemental purity of our compounds. The EDX spectra observed for each compound revealed peaks corresponding to manganese (Mn), cobalt (Co), iron (Fe) and oxygen (O), with the absence of any other impurity peaks (the peaks of Na and Si originate from adhesive tape made of silicone-based adhesive,
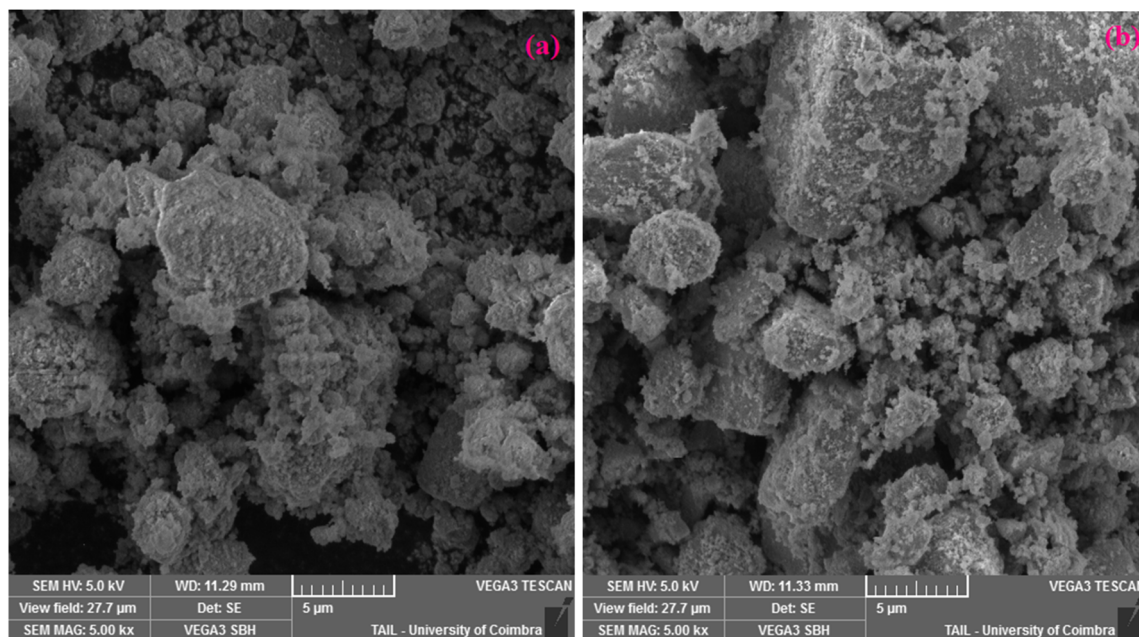

Fig. 3 SEM images of $Co_{0.33}Mn_{0.33}Fe_{2.33}O_4$ annealed at 300 °C (a) and 600 °C (b).
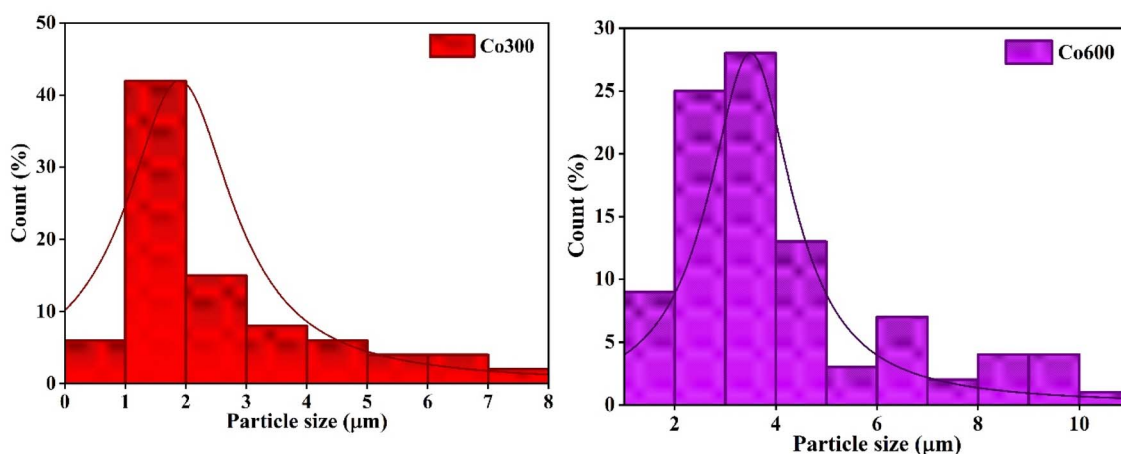
© 2025 The Author(s). Published by the Royal Society of Chemistry

Fig. 4 Histogram of the particle size distribution obtained by SEM image analysis of $Co_{0.33}Mn_{0.33}Fe_{2.33}O_4$ annealed at 300 °C (Co300) and 600 °C (Co600).

and the carbon peak originates from the sample support), thus confirming the high chemical purity of the prepared compounds. The results, presented in weight percentages and atomic percentages (Table 2), confirm the expected stoichiometry of our samples. The precise distribution of elements allows verification of the synthesis quality and material homogeneity, which are essential for interpreting the structural and functional properties.

Fig. 6 show the elemental maps of our Co300 and Co600 samples. These images reveal a uniform distribution of all the elements according to the initial concentrations during the preparation of the ferrites.[20]

3.3. Optical properties

3.3.1. Optical reflectance spectra. We recorded the scattered reflectance spectra of the compound $Co_{0.33}Mn_{0.33}Fe_{2.33}O_4$ annealed at 300 °C and 600 °C, at room temperature in the wavelength range (between 200 and 1700 nm). They are shown in Fig. 7. For the Co300 sample, reflectance is low in the UV range, suggesting maximum absorption in this range. In contrast, the reflectance values are high in the visible range, indicating strong optical scattering of this material in this region. However, when the annealing temperature is increased, the reflectance becomes high over the entire wavelength range, including the UV, with a marked increase compared with the Co300 sample. This phenomenon could be associated with crystal growth, as indicated by analysis of the morphology of these compounds.

3.3.2. Optical gap energy. The optical gap energy E_g is estimated using the Kubelka–Munk (KM) function $F(R)$[28] (4) given by:

$$F(R) = \frac{(1-R)^2}{2R} = \frac{\alpha}{s} \quad (4)$$

where R represents the scattered reflectance, S is the scattering factor (it is independent of wavelength) and α is the absorption coefficient, related to E_g by the Tauc relation[3] (5):

$$(\alpha h\nu)^n = A(h\nu - E_g) \quad (5)$$

where ν is the photon frequency, h is Planck's constant and n is a coefficient whose value depends on the nature of the transition. It is equal to 2 or $\frac{1}{2}$ if the transition is direct or indirect permitted and to 3 and $\frac{3}{2}$ if it is direct or indirect non-permitted respectively. It has been shown in the literature[30] that in compounds based on spinel ferrite and its alloys, the transitions are of the direct type, where the value of n is then equal to 2.

Therefore equations (4) and (5) give (6):

$$(F(R)h\nu)^2 = \frac{A}{s}\left(h\nu - E_g\right) \quad (6)$$

The plot of $(F(R)h\nu)^2$ as a function of the photon energies $h\nu$ and the extrapolation of the linear region of this curve to the X-axis (i.e. $(F(R)h\nu)^2 = 0$), as shown in Fig. 8, yields to the values of E_g. The obtained values for the bandgap width are estimated to 3.13 eV for Co300 and 2.45 eV for Co600. The gap energy decreases from 3.13 eV to 2.45 eV as the annealing temperature increases. Based on the X-ray diffraction results, we showed that the average crystallite size increases with increasing annealing temperature. This increase in crystallite size can influence the density of localized states, as the expansion or contraction of the optical bandgap correlates with the density of localized states. Consequently, this reduction in the band gap could be linked to the increase in the density of localized states.[31] On the other hand, the optical band gap is affected by the difference between the energy widths of tetrahedral and octahedral sites in ferrite structures. The division of the d-level to e_g and t_{2g} caused by a crystal field means that tetrahedral sites have a lower energy width than octahedral sites. The corresponding energy gap is given by the relation $\Delta_t = \frac{4}{9}\Delta_o$, with Δ_t and Δ_o representing the energy gap at these two sites respectively.[32,33] In the present study, it is likely that there is a repositioning of the cations on the sites following annealing at higher temperatures, leading to
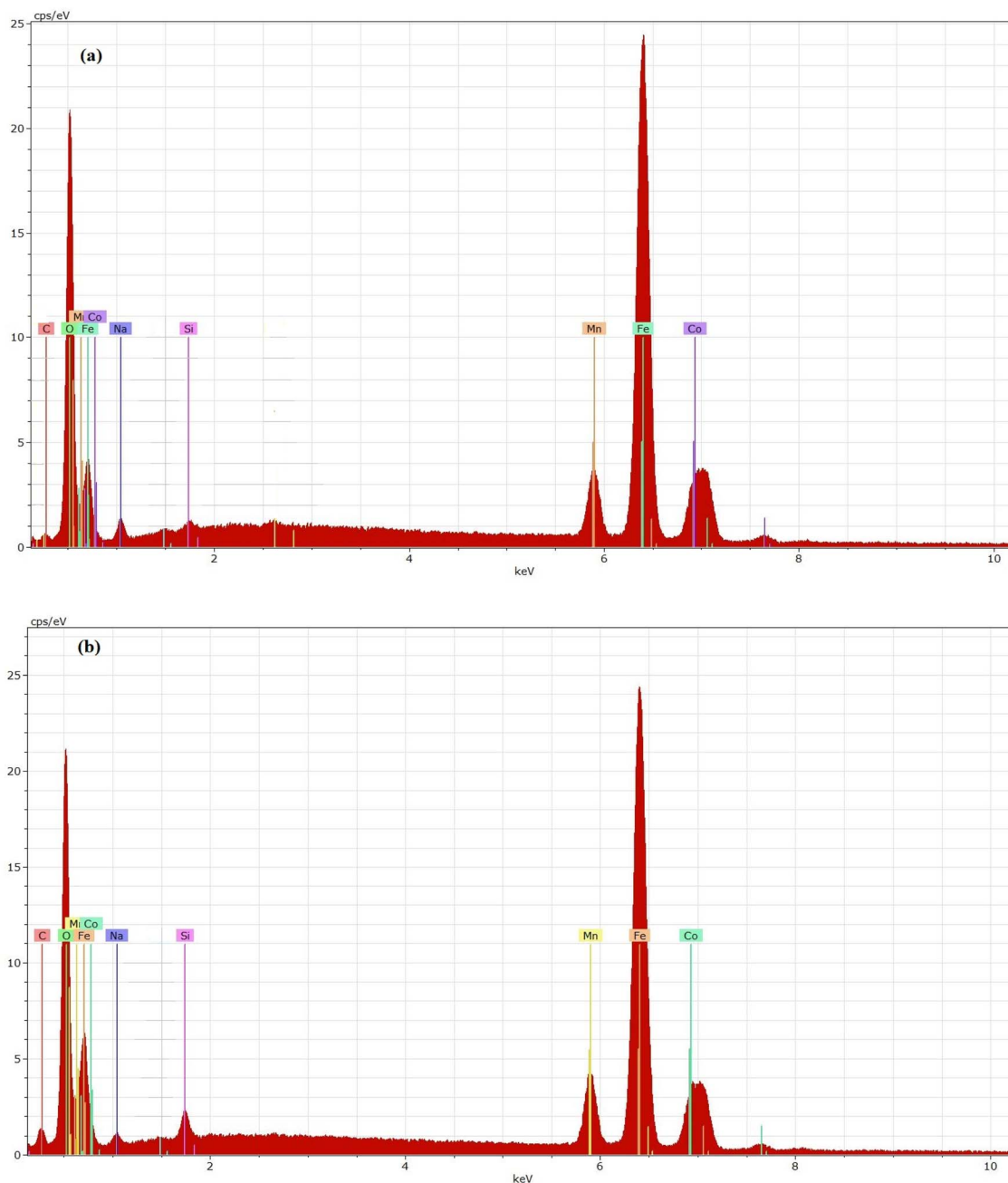
Fig. 5 EDX images of $Co_{0.33}Mn_{0.33}Fe_{2.33}O_4$ annealed at 300 °C (a) and 600 °C (b).

Table 2 Elemental distribution of $Co_{0.33}Mn_{0.33}Fe_{2.33}O_4$ ferrite obtained by EDX spectroscopy

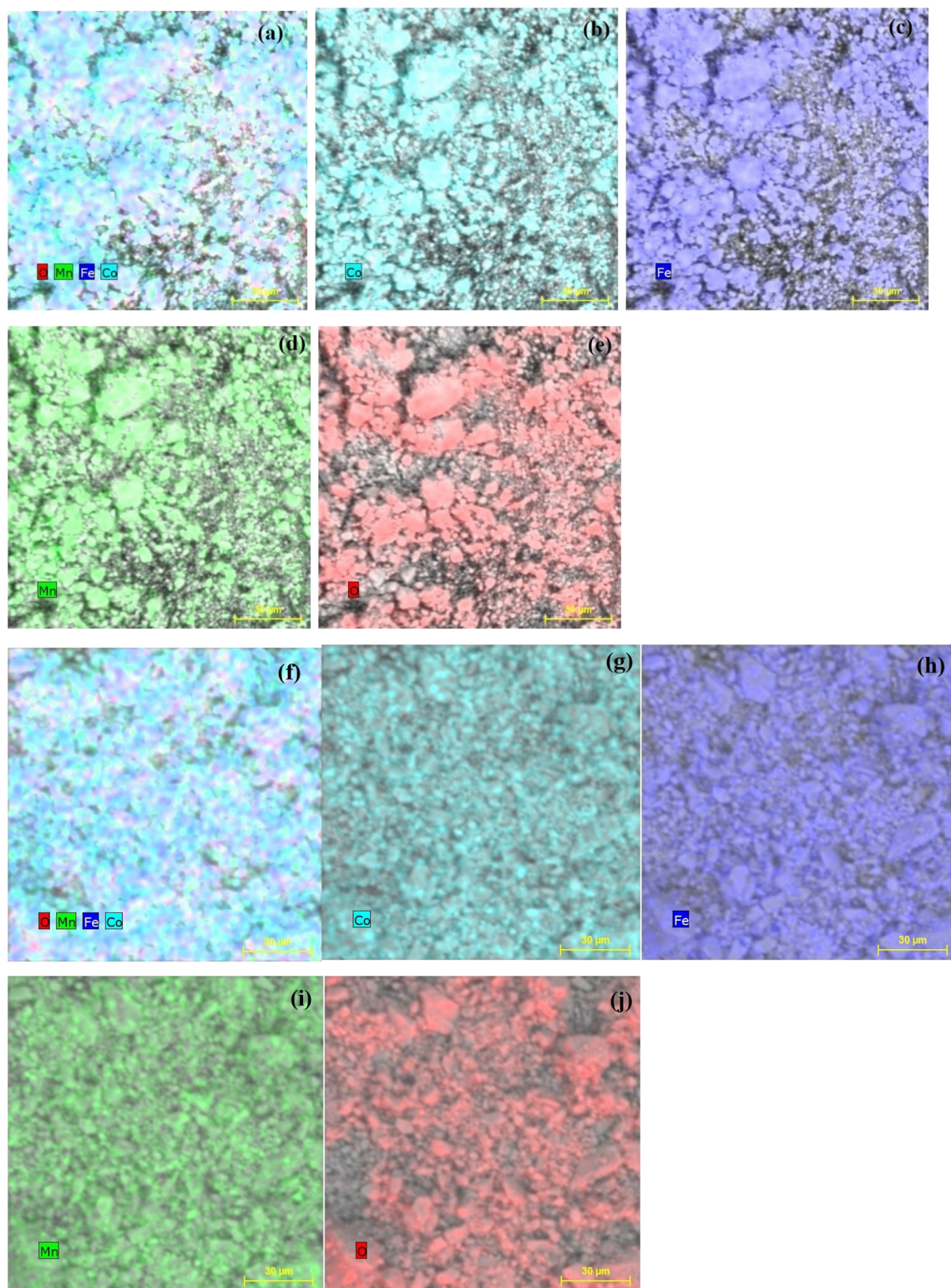| Element	Series	Atom. C [at%]		Norm. C [wt%]	
		Co300	Co600	Co300	Co600
Carbon (from sample support)	K-series	7.13	12.75	3.17	6.10
Oxygen	K-series	62.63	61.72	37.11	39.36
Sodium (from adhesive tape)	K-series	2.19	1.29	1.86	1.18
Silicon (from adhesive tape)	K-series	0.22	0.69	0.23	0.77
Manganese	K-series	2.28	2.09	4.63	4.57
Iron	K-series	22.96	18.78	47.50	41.80
Cobalt	K-series	2.45	2.61	5.53	6.13

Fig. 6 Elemental maps of $Co_{0.33}Mn_{0.33}Fe_{2.33}O_4$ annealed at 300 °C (a–e) and 600 °C (f–j).

a variation in the optical bandgap. The increase in annealing temperature in our $Co_{0.33}Mn_{0.33}Fe_{2.33}O_4$ sample probably led to the redistribution of Mn and/or Co ions from one site to another, thus decreasing the optical band gap due to the smaller value of Δ_t compared to Δ_o.[34] Theoretical studies based on density functional theory (DFT) strongly support this interpretation. Fritsch *et al.*[35] demonstrated that increasing the inversion degree in $ZnFe_2O_4$ modifies the distribution of
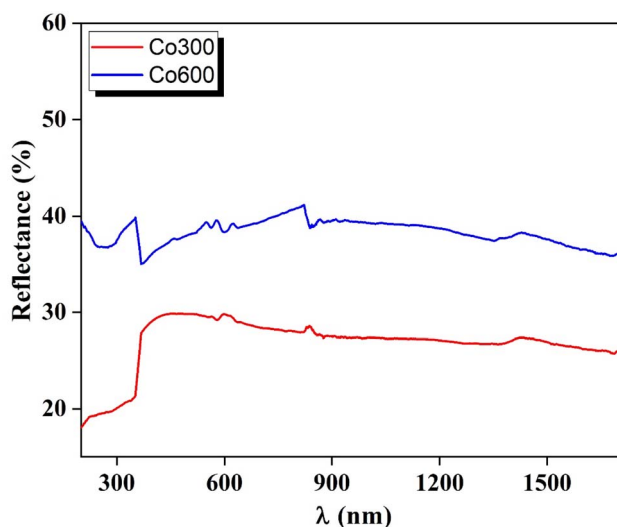
Fig. 7 Reflectance spectra of the compound $Co_{0.33}Mn_{0.33}Fe_{2.33}O_4$ annealed at 300 °C and 600 °C at room temperature in the wavelength range between 200 and 1700 nm.

electronic states and progressively narrows the band gap. Similarly, DFT + U calculations on inverse $NiFe_2O_4$ revealed an indirect gap of around 1.6 eV, sensitive to site occupancy and spin state.[36] Ulpe *et al.*[37] further showed that the magnitude of the band gap in MFe_2O_4 (M = Mn, Co, Ni, Zn) is governed by cation configuration, spin state, and orbital interactions. More recently, a DFT study on Mn–Zn substituted ferrites confirmed that cation redistribution between A and B sites alters the electronic band structure and decreases the band gap while maintaining semiconducting behavior.[38] These theoretical findings are consistent with our experimental results, suggesting that annealing-induced cation migration plays a central role in the observed reduction of the optical band gap.

To confirm that the type of gap is direct type, we have plotted the spectrum of variation of the first derivative of reflectance $\left(\dfrac{\mathrm{d}R}{\mathrm{d}\lambda}\right)$ as a function of wavelength (λ) (Fig. 9). We observe that the gap energy values deduced from the first-derivative method of reflectance are very close to those estimated by Tauc's law, which clearly confirms the direct nature of the gap.[39]

3.4. Dielectric proprieties

3.4.1. Real part of permittivity. Dielectric properties generally reveal details about polarization mechanisms present in samples. Fig. 10 shows the variation of the real part of permittivity (ε') as a function of frequency at different temperatures. It can be seen that at low frequencies, ε' shows higher values for both samples, commonly attributed to interfacial (Maxwell–Wagner) polarization caused by charge accumulation at grain boundaries, as observed in spinel ferrites.[40] This suggests that such materials could be promising for energy storage applications at lower frequencies. However, as frequency rises, ε' values generally decrease because dipoles and charge carriers cannot follow the rapidly alternating electric
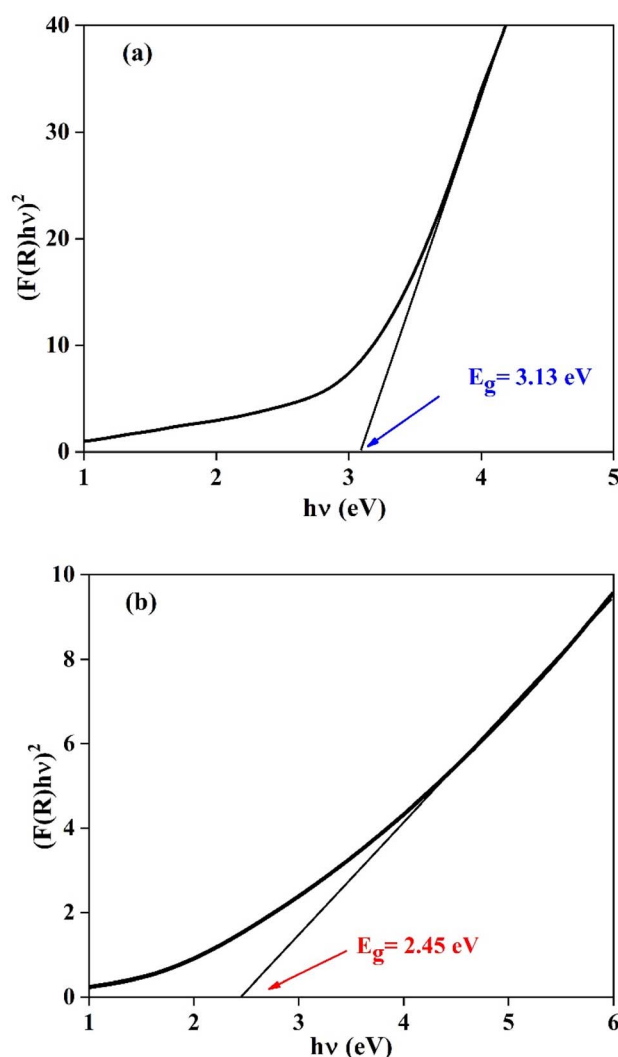

Fig. 8 Plot of $(F(R)h\nu)^2$ as a function of the photon energies $h\nu$ of $Co_{0.33}Mn_{0.33}Fe_{2.33}O_4$ annealed at 300 °C (a) and 600 °C (b).

field. An increase in ε' observed in certain frequency ranges indicates dielectric dispersion related to localized electronic states and hopping conduction mechanisms between these states, in agreement with Mott's model.[41,42] Furthermore, for Co300 (Fig. 10(a)), ε' decreases with temperature, then increases at a temperature equal to 420 K, indicating a metal–semiconductor transition linked to changes in carrier mobility or structural rearrangements. Similar temperature-dependent dielectric anomalies have been reported in cobalt ferrites.[43] However, for Co600 (Fig. 10(b)), ε' increases with temperature, reflecting thermal activation of the charge carriers, that enhances polarization *via* hopping conduction, as supported by experimental and theoretical studies.[44–46] These observations confirm that the dielectric behavior of these spinel ferrites results from the interplay of interfacial polarization, crystal field effects on electronic states, and charge hopping mechanisms.

3.4.2. Imaginary part of permittivity. Fig. 11 shows the frequency dependence of the imaginary part of the dielectric
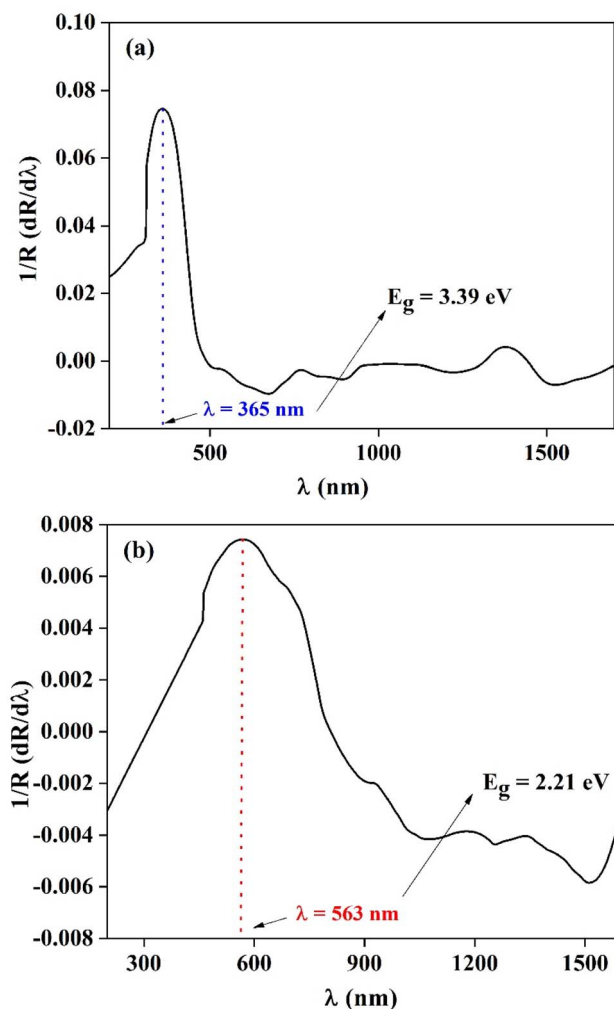
Fig. 9 Variation of the first derivative of reflectance $\left(\dfrac{\mathrm{d}R}{\mathrm{d}\lambda}\right)$ as a function of wavelength (λ) of $Co_{0.33}Mn_{0.33}Fe_{2.33}O_4$ annealed at 300 °C (a) and 600 °C (b).

Fig. 10 Frequency-dependent real (ε') part of the dielectric constant measured at different temperature for samples Co300 (a) and Co600 (b).

permittivity (ε'') for different temperatures. It is clear that the value of the imaginary part of the dielectric permittivity (ε'') is high at low frequencies. This effect may be due to an increase in carrier density[45,46] and interfacial polarization effects such as Maxwell–Wagner polarization.[40] These phenomena contribute to significant dielectric losses due to charge accumulation and relaxation processes at grain boundaries. However, at high frequencies it tends towards 0, indicating the inability of charge carriers and dipoles to follow the rapidly alternating electric field, leading to reduced energy dissipation. This behavior is consistent with dielectric dispersion caused by localized electronic states within the bandgap. It can be seen also that for Co300 (Fig. 11(a)), the value of the imaginary part of the dielectric permittivity (ε'') decreases with temperature and then increases, indicating a metal–semiconductor transition. This transition reflects changes in carrier mobility and possible structural rearrangements affecting the electronic structure. The redistribution of cations alters crystal field splitting of transition metal d-orbitals, creating localized states that
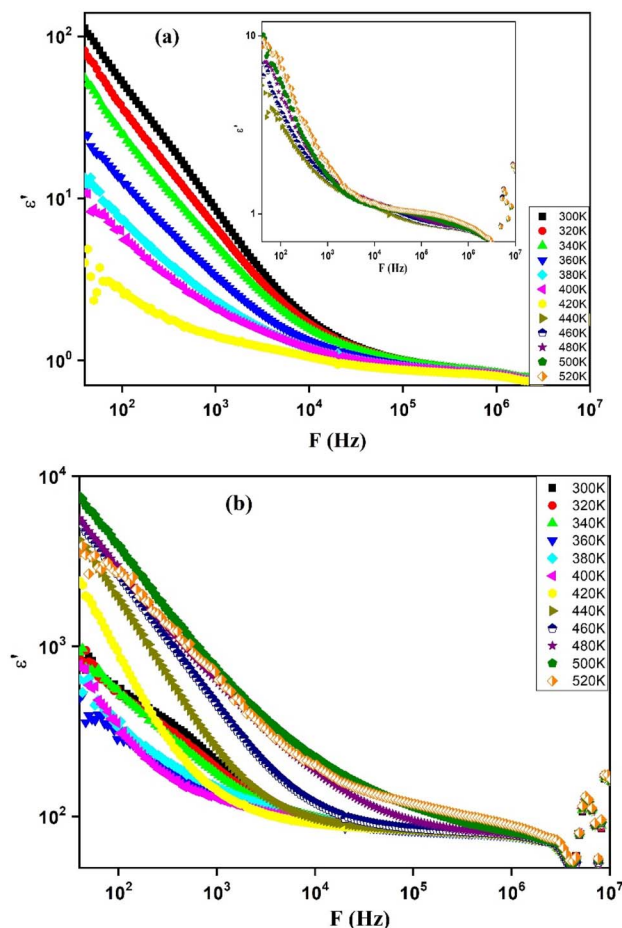
facilitate charge hopping mechanisms, which in turn influence dielectric losses.[44,47] In contrast, for Co600 (Fig. 11(b)), ε'' successively increases with temperature, providing evidence of semiconductor behavior characterized by thermally activated charge carriers enhancing dielectric losses *via* hopping conduction, as described by Mott's theory of conduction in localized states.[43,48]

3.4.3. Dielectric loss. Additionally, dielectric loss $\tan(\delta)$ is examined. This parameter defines the dispersion of electrical energy within a dielectric material when an electric field is applied, thereby facilitating an understanding of the efficiency of energy storage and transmission in electrical systems. This parameter is deduced from relation (7):

$$\tan(\delta) = \frac{\varepsilon''}{\varepsilon'} \tag{7}$$

Fig. 12 shows the frequency dependence of the dielectric loss at different temperatures. It can be seen that at low frequencies, $\tan(\delta)$ shows a high value. This can be explained by the existence of interfacial (Maxwell–Wagner) polarization caused by charge accumulation at grain boundaries, which results in an
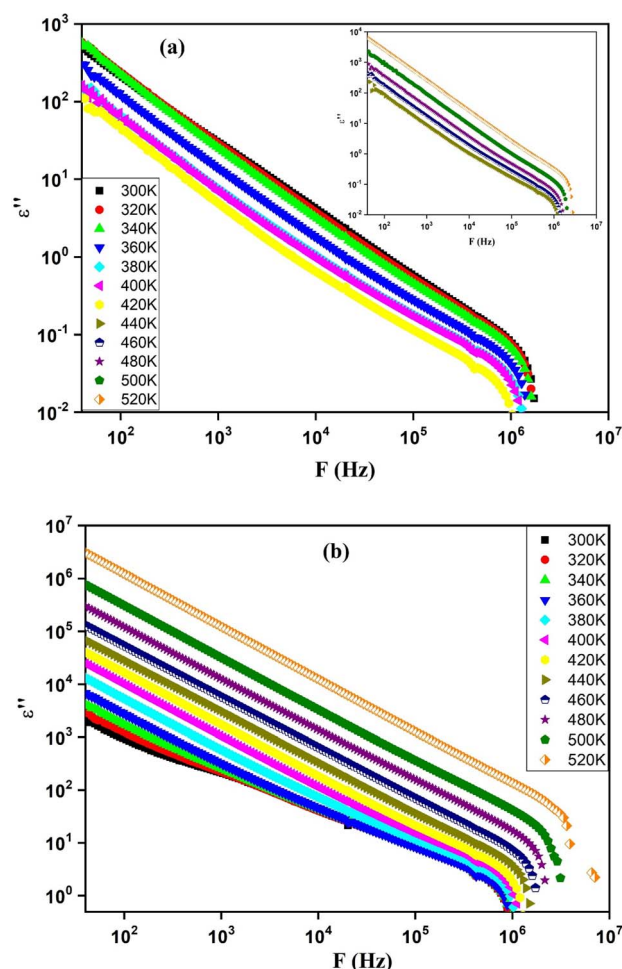
Fig. 11 Frequency-dependent imaginary (ε'') part of the dielectric constant measured at different temperature for samples Co300 (a) and Co600 (b).
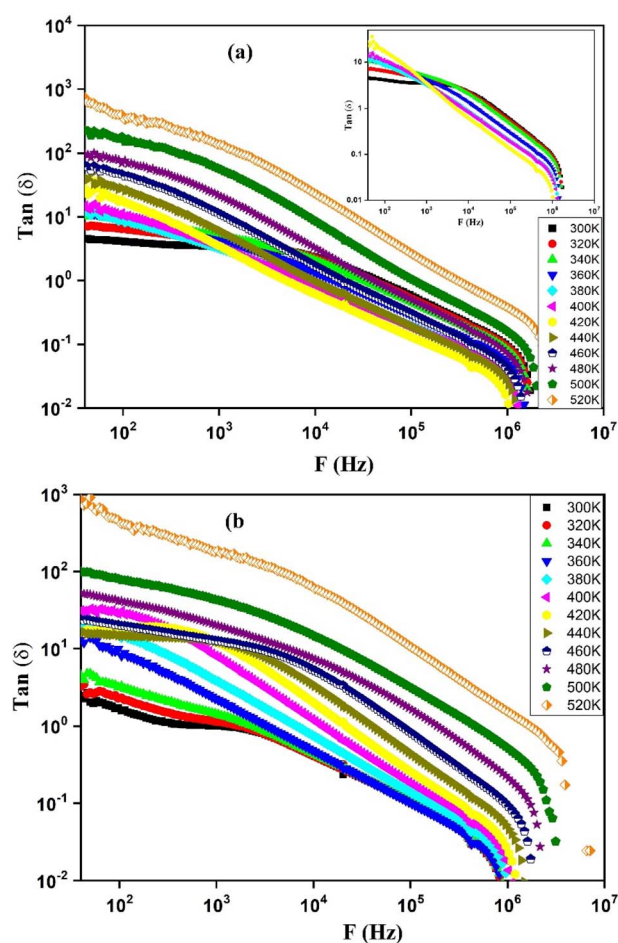

Fig. 12 Frequency-dependent dielectric loss factor measured at different temperature for samples Co300 (a) and Co600 (b).

increased energy demand to generate charge carrier mobility.[40] This polarization is strongly influenced by the local electronic structure, as cation redistribution modifies the crystal field splitting of transition metal d-orbitals, creating localized states that govern charge transport. As frequency increases, tan(δ) decreases. This variation can be attributed to the decreasing resistivity of the material, resulting in lower energy consumption of charge carrier flow.

Concerning the variation with temperature, tan(δ) increases with temperature in the low-frequency region for the Co300 sample (Fig. 12(a)) reflecting enhanced charge carrier hopping between localized states facilitated by thermal activation, consistent with the Mott hopping conduction model.[44,47] However, in the high-frequency region, tan(δ) decreases. Then, it increases above a transition temperature equal to 420 K, indicative of a metal–semiconductor transition altering the electronic structure and carrier dynamics. For the Co600 sample (Fig. 12(b)), there is a significant increase in dielectric loss as a function of temperature over the entire frequency range. This can be explained by the enhanced mobility of charge carriers and their accumulation at grain boundaries as a result of

increased temperature, which leads to an increase in dielectric loss.

3.4.4. Nyquist diagram. To identify the different contributions of microstructure to the conduction process in the $Co_{0.33}Mn_{0.33}Fe_{2.33}O_4$ compound annealed at 300 and 600 °C, we have plotted the Nyquist diagram or specific temperatures shown in Fig. 13.

For the Co300 sample (Fig. 13(a)), the Nyquist plot shows two semicircles corresponding to the grains and grain boundaries, with radii increasing with temperature. This behavior reflects enhanced charge carrier mobility and stronger interactions between microstructural features, consistent with the observed average grain size ($\sim$1.95 μm). The plot was modeled using two series RC circuits (($R_{gb} - CPE_{gb}$) for the grain boundaries and ($R_g - CPE_g$) for the grains), where the CPE accounts for deviations from ideal capacitive behavior due to microstructural heterogeneities.[49]

For Co600 (Fig. 13(b)), three semicircles are observed at low temperatures (300 and 340 K), corresponding to the grains, grain boundaries, and electrode interface, while above 340 K, only two arcs appear and their radii decrease with increasing temperature. This behavior is consistent with grain growth after
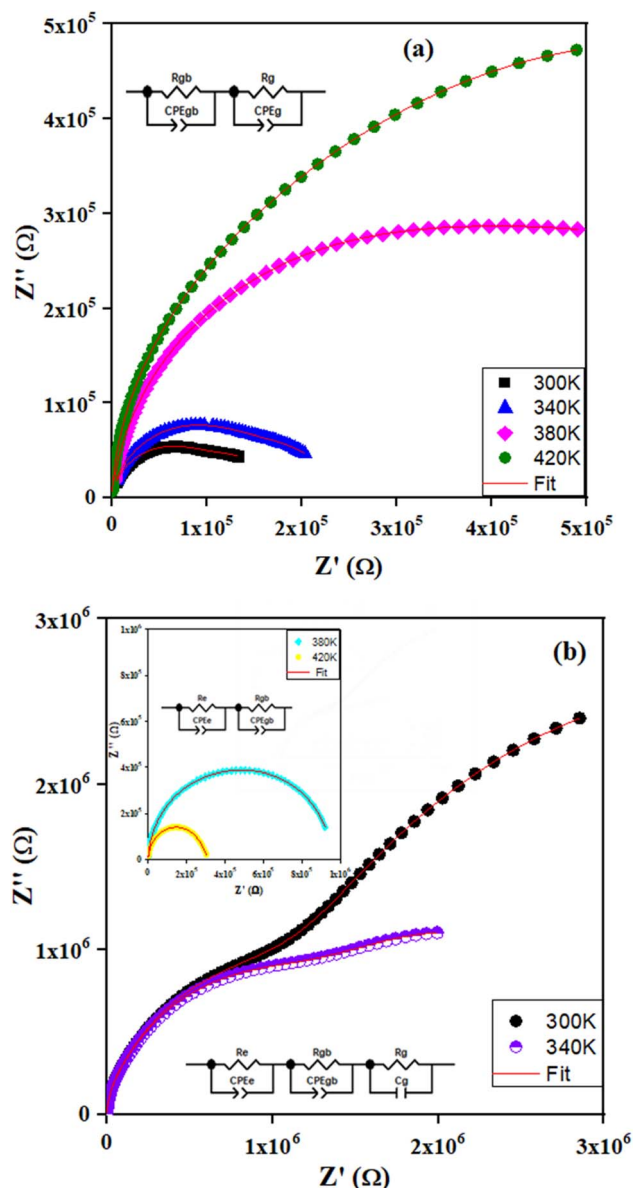
Fig. 13 Nyquist diagram and associated electrical circuits for samples Co300 (a) and Co600 (b).

$Fd\bar{3}m$. The intensity of the X-ray diffraction peaks increases with the annealing temperature which signifies that the crystallinity is improved. The morphological study shows an increase in grain size from 1.95 μm to 3.53 μm with increasing annealing temperature. EDX analysis reveals the presence of all elements and the absence of any impurities. These proprieties proved the efficiency of the preparation process. The optical results show a decrease in the bandgap width with increasing annealing temperature, from 3.13 eV to 2.45 eV indicating that this reduction in the bandgap could be related to the increase in the density of localized states in our material. Furthermore, dielectric characterization revealed a high dielectric constant associated with low loss, highlighting the material's potential for the design of miniaturized capacitors offering increased energy storage density and improved efficiency. In addition, these characteristics make the material suitable for electromagnetic absorbers operating in the GHz range, useful for reducing interference in electronic devices. However, limitations remain, including thermal stability, which must be improved to ensure long-term performance, as well as the need to adapt the synthesis process for large-scale production of thin films with optimal reproducibility. Future work will also focus on developing thin films using suitable techniques to enable the effective integration of these ferrites into electronic devices and industrial applications.

Conflicts of interest

The authors declare that they have no known competing financial interests or personal relationships that could have appeared to influence the work reported in this paper.

Data availability

Data are available upon request to the authors.

Acknowledgements

References

1 S. Xu, X. Zhang, T. Zheng, Z. Zhao, C. Shang, Z. Hu, M. Dong, Y. Qiao, C. Bai, X. Zhang, G. Sun and X. Wang, *J. Mater. Sci. Technol.*, 2026, **252**, 57–90.

2 X. Tian, Y. Zhao, T. Gu, Y. Guo, F. Xu and H. Hou, *Mater. Sci. Eng., A*, 2022, **849**, 143–485.

3 I. Soudani, K. Ben Brahim, A. Oueslati, A. Aydi, K. Khirouni, A. Benali, E. Dhahri and M. A. Valente, *RSC adv.*, 2023, **13**, 9260–9272.

4 A. Benali, M. Bejar, E. Dhahri, M. Sajieddine, M. P. F. Graça and M. A. Valente, *Mater. Chem. Phys.*, 2015, **149**, 467–472.

5 L. Saher, A. Benali, S. Haddad, E. Dhahri, M. P. F. Graça, B. F. O. Costa, L. A. Helguero and A. M. S. Silva, *Crystals*, 2025, **15**, 1–14.

annealing (∼3.53 μm), which reduces the resistance of the grains. The Nyquist plots were fitted with three series circuits at low temperature ($R_e − CPE_e$, $R_{gb} − CPE_{gb}$, $R_g − C_g$) and two circuits at higher temperatures ($R_{gb} − CPE_{gb}$, $R_g − C_g$). The capacitance values allow identification of each component, with the electrode effect exhibiting the highest capacitance, followed by grain boundaries and grains, confirming that microstructure and annealing directly influence the electrical response of the ferrite.[50]

4. Conclusion

$Co_{0.33}Mn_{0.33}Fe_{2.33}O_4$ was synthesized by the coprecipitation method. Structural analysis by X-ray diffraction shows that our compound crystallizes in the cubic structure of the space group

6 I. El Heda, J. Massoudi, R. Dhahri, E. Dhahri, F. Bahri and B. F. O. Costa, *J. Alloys Compd.*, 2023, **931**, 167479.

7 H. Javed, A. Rehman, S. Mussadiq, M. Shahid, M. A. Khan, I. Shakir, P. O. Agboola, M. F. A. Aboud and M. F. Warsi, *Synth. Met.*, 2019, **254**, 1–9.

8 K. Wei, H. X. Huai, B. Zhao, J. Zheng, G. Q. Gao, X. Y. Zheng and C. C. Wang, *Sens. Actuators, B*, 2022, **369**, 132279.

9 P. Tartaj, S. Veintemillas-Verdaguer, T. Gonzalez-Carreño and C. J. Serna, *Magnetic Nanoparticles in Biosensing and Medicine*, 2019, vol. 36, pp. 52–67.

10 W. Fontijn, P. Van der Zaag and M. Devillers, *Phys. Rev. B*, 1997, **56**, 5432–5442.

11 J. Philip, P. D. Shima and B. Raj, *Appl. Phys. Lett.*, 2008, **92**, 10–13.

12 L. Kaufner, R. Cartier, R. Wüstneck, I. Fichtner, S. Pietschmann, H. Bruhn, D. Schütt, A. F. Thünemann and U. Pison, *Nanotechnology*, 2007, **18**, 115–710.

13 Y. Chen, J. E. Snyder, C. R. Schwichtenberg, K. W. Dennis, R. W. McCallum and D. C. Jiles, *Digests of the Intermag Conference*, 1999, pp. 3652–3654.

14 H. G. Zhang, W. H. Wang, E. K. Liu, X. D. Tang, G. J. Li, J. L. Chen, H. W. Zhang and G. H. Wu, *Phys. Status Solidi B*, 2013, **250**, 1287–1292.

15 S. Othmani, R. Blel, M. Bejar, M. Sajieddine, E. Dhahri and E. K. Hlil, *Solid State Commun.*, 2009, **149**, 969–972.

16 A. Benali, L. Saher, M. Bejar, E. Dhahri, M. F. P. Graca, M. A. Valente, P. Sanguino, L. A. Helguero, K. Bachari, A. M. S. Silva and B. F. O. Costa, *J. Mater. Sci.: Mater. Electron.*, 2023, **34**, 1–17.

17 R. M. Kershi, *Mater. Chem. Phys.*, 2020, **248**, 122–941.

18 R. G. E. Gharibshahi, B. D. Young and S. Bhalla, *J. Mater. Sci. Technol.*, 2020, **57**, 180–187.

19 G. Vishnu, S. Singh, N. Kaul, P. C. Ramamurthy, T. S. S. K. Naik, R. Viswanath, V. Kumar, H. S. Bhojya Naik, A. Prathap, H A. Anil Kumara, J. Singh and N. A. Khan, *Environ. Res.*, 2023, **235**, 116598.

20 R. Jasrotia, N. Kumari, R. Verma, Suman, S. K. Godara, J. Ahmed, S. M. Alshehri, B. Pandit, S. Kumar, Himanshi, S. Sharma, Kirti and P. K. Maji, *J. Rare Earths*, 2023, **41**, 1763–1770.

21 M. Atif, M. Idrees, M. Nadeem, M. Siddique and M. W. Ashraf, *RSC Adv.*, 2016, **6**, 20876–20885.

22 P. Sowjanya, N. P. Kumar, A. Chelvane and M. V. R. Reddy, *Mater. Sci. Eng., B*, 2022, **279**, 115674.

23 R. Ramadan and A. S. Shafaay, *J. Mater. Sci.: Mater. Electron.*, 2024, **35**, 1–20.

24 A. T. Raghavender and K. M. Jadhav, *Bull. Mater. Sci.*, 2009, **32**, 575–578.

25 K. Luo, Q. Fu, X. Liu, R. Zhao, Q. He, B. Hu, Z. An, W. Yang, Y. Zhang, S. Zhang, J. Zhan and J. Duan, *Opt Laser. Eng.*, 2024, **174**, 107–970.

26 J. Othmani, S. Hcini, J. Massoudi, M. L. Bouazizi, A. Dhahri, K. Khirouni and E. Dhahri, *Eur. Phys. J. Plus*, 2025, (accepted).

27 I. El Heda, J. Massoudi, R. Dhahri, F. Bahri, E. Dhahri, K. Khirouni, B. F. O. Costa and O. M. Lemine, *Phys. E*, 2024, **158**, 115904.

28 J. Massoudi, M. Smari, K. Nouri, E. Dhahri, K. Khirouni, S. Bertaina, L. Bessais and E. Hlil, *RSC Adv.*, 2020, **10**, 34556–34580.

29 S. M. Chavan, M. K. Babrekar, S. S. More and K. M. Jadhav, *J. Alloys Compd.*, 2010, **507**, 21–25.

30 S. M. Ansari, D. Phase, Y. D. Kolekar and C. V. Ramana, *Mater. Sci. Eng., B*, 2024, **300**, 117134.

31 M. Zulqarnain, S. S. Ali, C. Cheng, K. Nadeem, M. Rizwan and T. Anwar, *J. Magn. Magn. Mater.*, 2023, **565**, 170252.

32 B. Zhou, Y. W. Zhang, Y. J. Yu, C. S. Liao, C. H. Yan, L. Y. Chen and S. Y. Wang, *Phys. Rev. B*, 2003, **68**, 1–8.

33 R. G. Burns, *Mineralogical Applications of Crystal Field Theory*, Cambridge university press, 1993.

34 D. Sharma and N. Khare, *Appl. Phys. Lett.*, 2014, **105**, 32–404.

35 D. Fritsch, *J. Phys.: Condens. Matter*, 2018, **30**(9), 095502.

36 J. Wangchhuk and S. R. Meher, *Phys. Lett. A*, 2022, **443**, 128202.

37 A. C. Ulpe, K. C. L. Bauerfeind and T. Bredow, *ACS Omega*, 2019, **4**, 4138–4146.

38 J. Li, K. K. Cheepurupalli, N. J. English and S. Bandaru, *Mater. Sci.*, 2025, **36**, 48–530.

39 I. El Heda, J. Massoudi, R. Dhahri, E. Dhahri, F. Bahri, L. H. Omari and J. F. M. L. Mariano, *Mater. Chem. Phys.*, 2023, **296**, 1–14.

40 Z. H. Wang, S. C. Jiang, X. Xiong, R. W. Peng and M. Wang, *Appl. Phys. Lett.*, 2016, **108**, 261107.

41 T. Katayama, A. Chikamatsu, Y. Hirose, H. Kumigashira, T. Fukumura and T. Hasegawa, *J. Phys. D: Appl. Phys.*, 2014, **47**(13), 135304.

42 N. F. Mott, *J. Non-Cryst. Solids*, 1978, **28**, 147–158.

43 Y. Mizuta, *J. Magn. Magn. Mater.*, 2017, **431**, 209–213.

44 W. J. Kim, J. H. Gruenewald, T. Oh, S. Cheon, B. Kim, O. B. Korneta, H. Cho, D. Lee, Y. Kim, M. Kim, J. G. Park, B. J. Yang, A. Seo and T. W. Noh, *Phys. Rev. B*, 2018, **98**, 1–9.

45 C. Ben Makhlouf, S. Bouzidi, A. Gassoumi, A. Selmi, F. Hcini, S. Hcini and M. Gassoumi, *J. Sol–Gel Sci. Technol.*, 2024, **110**, 859–874.

46 M. M. Bouzayani, I. Soudani, M. Ben Abdessalem, S. Znaidia, A. Oueslati and A. Aydi, *J. Mater. Sci.: Mater. Electron.*, 2024, **35**, 1–17.

47 T. F. T. Katayama, A. Chikamatsu, Y. Hirose and H. Kumigashira, *J. Phys. D: Appl. Phys.*, 2014, **47**, 135–304.

48 N. Ponpandian, P. Balaya and A. Narayanasamy, *J. Phys.: Condens. Matter*, 2002, **14**, 3221–3237.

49 R. K. Hona, R. Dhaliwal and G. S. Thapa, *Appl. Sci.*, 2022, **12**, 29–30.

50 J. Yang, W. Bai, Y. Zhang, C. G. Duan, J. Chu and X. Tang, *J. Phys.: Condens. Matter*, 2023, **35**, 463001.